PHYSICS

RASER MRI: Magnetic resonance images formed spontaneously exploiting cooperative nonlinear interaction

Sören Lehmkuhl[1,2]*, Simon Fleischer[3], Lars Lohmann[3], Matthew S. Rosen[4,5], Eduard Y. Chekmenev[6,7], Alina Adams[3], Thomas Theis[2,8,9]*, Stephan Appelt[3,10]*

The spatial resolution of magnetic resonance imaging (MRI) is limited by the width of Lorentzian point spread functions associated with the transverse relaxation rate $1/T_2^*$. Here, we show a different contrast mechanism in MRI by establishing RASER (radio-frequency amplification by stimulated emission of radiation) in imaged media. RASER imaging bursts emerge out of noise and without applying radio-frequency pulses when placing spins with sufficient population inversion in a weak magnetic field gradient. Small local differences in initial population inversion density can create stronger image contrast than conventional MRI. This different contrast mechanism is based on the cooperative nonlinear interaction between all slices. On the other hand, the cooperative nonlinear interaction gives rise to imaging artifacts, such as amplitude distortions and side lobes outside of the imaging domain. Contrast mechanism and artifacts are explored experimentally and predicted by simulations on the basis of a proposed RASER MRI theory.

INTRODUCTION

RASER [radio-frequency (RF) amplification by stimulated emission of radiation], also referred to as Zeeman maser, is a nuclear magnetic resonance (NMR) phenomenon as a result of stimulated nuclear spin transitions. RASERs have been investigated using hyperpolarized rare gases (*1*–*4*) as well as ^{1}H, ^{17}O, and even ^{27}Al spins in liquids and solids (*5*–*9*). Multimode RASERs enable comagnetometry, which, in turn, allows for precision measurements (*10*–*13*). In addition, multimode RASER activity gives insight into fundamental phenomena in nonlinear mathematics (*14*) and synergetics (*15*) such as line collapse, multiple-period doubling, intermittence, and chaos (*4*, *12*, *16*). Most recently, the parahydrogen (p-H_2) pumped (*17*, *18*) RASER has been established (*12*, *16*, *19*–*21*), by creating strong population inversions directly in room-temperature solutions. RASER magnetic resonance imaging (MRI) is associated with an alternative contrast mechanism than standard MRI, and it appears natural to wonder whether it could serve as a means to overcome fundamental limits of Lorentzian-based point spread functions (PSFs) in MRI (*22*, *23*).

The spatial resolution of MRI is limited by the width $w = 1/(\pi T_2^*)$ of the Lorentzian PSF. Here, we show that nonlinearly coupled slices can spontaneously form an image out of nuclear spin noise, as an alternative to the superposition of uncoupled Lorentzian PSFs. We describe previously unknown nonlinear MRI physics in a p-H_2 RASER while noting that nonlinear spin evolution in the presence of a gradient including radiation damping effects and dipolar fields has been reported before (*24*–*26*). We note that other hyperpolarization techniques may be used for RASER MRI as described here (*7*).

Conventional MRI uses spin or gradient echoes of nuclear magnetization that need to be excited with RF pulses. An interesting alternative is spin noise imaging, which measures projections without external RF excitation and fast gradient switching (*27*). Spin noise imaging does not require any initial hyperpolarization procedure but requires cryogenically cooled NMR probes and averaging to compensate for the low signal-to-noise ratio (SNR ~ 1).

The system under study here uses hyperpolarized samples in combination with an external high Q resonator at room temperature (*28*), thereby achieving an SNR of >200 in a single scan. The spontaneous RASER burst, which forms in the absence of external RF excitation, reflects the superposition of nonlinearly coupled slices. The corresponding spectrum (RASER MRI) of the burst reports on the spatial distribution of the samples spin number density and can have complicated and distorted shapes. On the other side, the image is very sensitive to local variations in the input profile. Therefore, RASER MRI entails new MRI physics challenges and opportunities caused by the nonlinear coupling.

In the presented work, RASERs emerge when placing a proton spin 1/2 ensemble with a large initial population inversion $d_0 = N_2 - N_1$, above the RASER threshold $d_{th} = 4\,V_s/(\mu_0 \hbar \gamma_H^2\, T_2^* Q)$ in a resonant LC circuit with quality factor Q. In this system, N_2 and N_1 are the populations of the corresponding Zeeman levels 2 and 1; V_s is the sample volume; and μ_0, $\hbar$, and γ_H denote the vacuum permeability, Planck's constant, and the proton gyromagnetic ratio, respectively. For RASER MRI, the proton spins are first pumped into a state of highly negative spin polarization P_H. This corresponds to a positive d_0 value, which is assumed to be several orders of magnitude above the RASER threshold d_{th}. An equivalent and convenient way to characterize the threshold condition for one singular mode is given by $\varepsilon = d_0/d_{th} = T_2^*/\tau_{rd} \gg 1$ (*29*, *30*), where ε is a dimensionless

[1]Institute of Microstructure Technology, Karlsruhe Institute of Technology, 76344 Eggenstein-Leopoldshafen, Germany. [2]Department of Chemistry, North Carolina State University, Raleigh, NC 27606, USA. [3]Institute of Technical and Macromolecular Chemistry, RWTH Aachen University, 52056 Aachen, Germany. [4]Massachusetts General Hospital, A. A. Martinos Center for Biomedical Imaging, Boston, MA 02129, USA. [5]Department of Physics, Harvard University, Cambridge, MA 02138, USA. [6]Department of Chemistry, Integrative Biosciences (IBio), Karmanos Cancer Institute (KCI), Wayne State University, Detroit, MI 48202, USA. [7]Russian Academy of Sciences, Leninskiy Prospekt 14, Moscow 119991, Russia. [8]Department of Physics, North Carolina State University, Raleigh, NC 27695, USA. [9]Joint Department of Biomedical Engineering, University of North Carolina at Chapel Hill and North Carolina State University, Raleigh, NC 27695, USA. [10]Central Institute for Engineering, Electronics and Analytics – Electronic Systems (ZEA-2), Forschungszentrum Jülich GmbH, D-52425 Jülich, Germany.
*Corresponding author. Email: lehmkuhl@kit.edu (S.L.); ttheis@ncsu.edu (T.T.); st.appelt@fz-juelich.de (S.A.)

quantity. Note that ε is the enhancement above the RASER threshold, not above thermal nuclear spin polarization. The radiation damping rate is given by $\tau_{rd}^{-1} = \mu_0 \hbar \gamma_H^2 Q\, d_0/(4\, V_s)$, which includes inverted states (positive d_0), and has been studied extensively in NMR spectroscopy (*24*, *29*, *31*–*33*).

To understand how the RASER can be used for MRI, we introduce an analysis of the RASER action in the presence of a magnetic field gradient G_z. The gradient creates a frequency range $\Delta = \gamma_H \cdot G_z \cdot L$ that spans the image domain of the object of length L (section S1). The initial nuclear spin population inversion is spread over the imaging domain Δ and is given by $d_0 = \int_{\nu_0-\Delta/2}^{\nu_0+\Delta/2} \rho_d(\nu)\, d\nu$, where $\rho_d(\nu)$ is the population inversion density and ν_0 is the off-resonance frequency in the center of the imaging domain. The integrand $\rho_d(\nu)d\nu$ can be described as the number of negatively polarized spins in the frequency interval $[\nu, \nu + d\nu]$. Given a profile $\rho_d(\nu)$, a total RASER MRI signal emerges spontaneously out of nuclear spin noise.

To generate a system where a numerical evaluation is feasible, we divide the image domain Δ into $N = \Delta/\delta\nu$ individual slices. To avoid numerical artifacts, the distance δν between consecutive slices has to be chosen small enough. Specifically, $\delta\nu < w$ has to be fulfilled, where $w = 1/(\pi T_2^*)$ is the natural linewidth. Furthermore, to estimate whether a given d_0 is RASER active in a given gradient G_z, we also introduce the threshold population density $\rho_d^{th} = d_{th}/w$ as used below.

To calculate the dynamics of the nonlinearly coupled slices, each slice $\mu = 1, \ldots, N$ is characterized by an initial population inversion $d_\mu(0) = \int_{\nu_0-\Delta/2+(\mu)\delta\nu}^{\nu_0-\Delta/2+(\mu-1)\delta\nu} \rho_d(\nu)\, d\nu$. With a given initial $d_\mu(0)$, the time evolution of the RASER modes or slices can be modeled by a set of $\mu = 1, \ldots, N$ nonlinearly coupled differential equations for the population inversion d_μ and the transverse spin component $\alpha_\mu = A_\mu \exp(i\phi_\mu)$

$$\dot{d}_\mu = -\frac{d_\mu}{T_1} - 4\beta \sum_{\sigma,\tau=1}^{N} A_\sigma A_\tau \cos(\phi_\sigma - \phi_\tau) \quad (1)$$

$$\dot{A}_\mu = -\frac{A_\mu}{T_2^*} + \beta\, d_\mu \sum_{\tau=1}^{N} A_\tau \cos(\phi_\tau - \phi_\mu) \quad (2)$$

$$\dot{\phi}_\mu = 2\pi\{\nu_0 - 0.5\,[\Delta - \delta\nu(2\mu - 1)]\} + \beta \frac{d_\mu}{A_\mu} \sum_{\tau=1}^{N} A_\tau \sin(\phi_\tau - \phi_\mu) \quad (3)$$

$$d_\mu(0) = \int_{\nu_0-\Delta/2+\mu\delta\nu}^{\nu_0-\Delta/2+(\mu-1)\delta\nu} \rho_d(\nu)\, d\nu \quad (4)$$

The coupling constant β is given as $\beta = \mu_0 \hbar \gamma_H^2 Q/(4\, V_s)$. The model for RASER MRI represented by Eqs. 1 to 4 is formulated in the rotating frame (for a complete derivation, see section S1) and is a modification of the existing multimode RASER theory (*12*, *16*). The modifications comprise the initial boundary conditions for $d_\mu(0)$ in Eq. 4, the absence of pumping in Eq. 1, and the definition of the slice frequencies in Eq. 3. Numerical simulations of Eqs. 1 to 4 reveal three important invariance principles for RASER MRI: Provided that $\delta\nu << w$ and $T_1 >> T_2^*$, the shape of the RASER images is independent of (i) the value of the slicing δν, (ii) the longitudinal relaxation time T_1, and (iii) the values of the initial conditions $A_\mu(0)$ and $\phi_\mu(0)$ (see section S6). According to the invariance principle (iii), the shape of the RASER image is the same, irrespective that the initial conditions for $A_\mu(0)$ and $\phi_\mu(0)$ are random values (i.e., nuclear spin noise) or a weak RF pulse with fixed values for $A_\mu(0)$ and $\phi_\mu(0)$. The three invariance principles are crucial for RASER MRI, because they guaranty reproducibility of RASER MRI.

Certain processes can be identified by examining the dynamics described by Eqs. 1 to 3: The population inversion of a given mode μ in Eq. 1 decays with the rate $1/T_1$ and is decreased by the rate given by the sum over all quadratic terms $-4\beta A_\sigma A_\tau \cos(\phi_\sigma - \phi_\tau)$. In turn, the amplitude of A_μ in Eq. 2 decays with the rate $1/T_2^*$ and increases for $\tau = \mu$ with the rate βd_μ. The last term on the right side of Eq. 2, $\beta d_\mu \sum_{\tau=1}^{N} A_\tau \cos(\phi_\tau - \phi_\mu)$ for $\tau \neq \mu$, involves a sum over all other amplitudes $A_\tau \cos(\phi_\tau - \phi_\mu)$. This sum can be a growth or decay rate for A_μ, depending on the specific values of all other phase differences $\phi_\tau - \phi_\mu$. The collective action of all modes strongly influences the amplitude and sign of the rate dA_μ/dt, which defines the amplitudes A_μ of the final image.

The spatial encoding of each slice $\mu = 1, \ldots, N$ is reflected by the first term in Eq. 3, where each slice is oscillating at the angular frequency $\omega_\mu = 2\pi(\nu_0 - 0.5\,(\Delta - \delta\nu(2\mu - 1)))$. Apart from this linear evolution of ϕ_μ with time t, there is a nonlinear collective term $(\beta\, d_\mu/A_\mu) \sum_{\tau=1}^{N} A_\tau \sin(\phi_\tau - \phi_\mu)$, which is responsible for synchronism. Equation 3 is analogous to Kuramoto's model of synchronized oscillators (*34*–*36*). The dynamics of RASER MRI given by Eqs. 1 to 4 can be described by a collection of synchronized oscillators or slices with distinct angular frequencies ω_μ, where the amplitude A_μ of each oscillator depends on the self-organization controlled by the collective interaction with all other slices. Therefore, the derivative of the amplitude of each slice depends on the mean-field amplitude produced by all other slices.

Last, the total RASER signal is obtained by the sum of all transverse spin components $\mathrm{Sig}(t) = N^{-1/2} \sum_{\mu=1}^{N} \mathrm{Re}(\alpha_\mu) = N^{-1/2} \sum_{\mu=1}^{N} A_\mu \mathrm{Re}(\exp[i\phi_\mu])$, where $N^{-1/2}$ is a normalization constant. Here, we focus on the difference between the concept of single PSFs to analyze conventional magnetic resonance image formation and the collective mean-field approach, which is the basis of RASER MRI. Numerical solutions of Eqs. 1 to 4 are evaluated (see Fig. 1) to highlight the difference of the spin dynamics for a single RASER slice and the collective behavior of coupled slices.

The simplest case is shown in Fig. 1A for $N = 1$ and $T_1 = \infty$, where the numerically evaluated form matches the exact solution introduced by Mao *et al.* (*31*, *37*, *38*) and discussed by others (*39*, *40*). The corresponding phased and absolute spectra of $\alpha = \alpha_1$ are displayed Fig. 1A (bottom right). For this case, $T_1 = \infty$, the PSF is a hyperbolic secant with width w_{sech} (section S2 and eq. S19). Close to the threshold, such a PSF is narrower than the Lorentzian NMR linewidth $w = 1/(\pi T_2^*)$, because the RASER signal involves dedamping.

No exact solution exists for a finite T_1, but the MR signal represents an asymmetrically shaped PSF (Fig. 1B and section S3). The linewidth w_{as} in the spectrum is slightly broader compared to the symmetric case (Fig. 1A) but still smaller than w.

Here, we include both the effects of finite T_1 and the nonlinear interactions between N slices formed in the presence of a gradient. In contrast to standard MRI, the image contrast and the spatial resolution cannot be explained by independent individual PSFs. Each slice is sensitive to the collective action of all slices, which makes RASER imaging highly sensitive to local variations in d_μ (section S4A), providing interesting avenues for future investigations for RASER MRI.

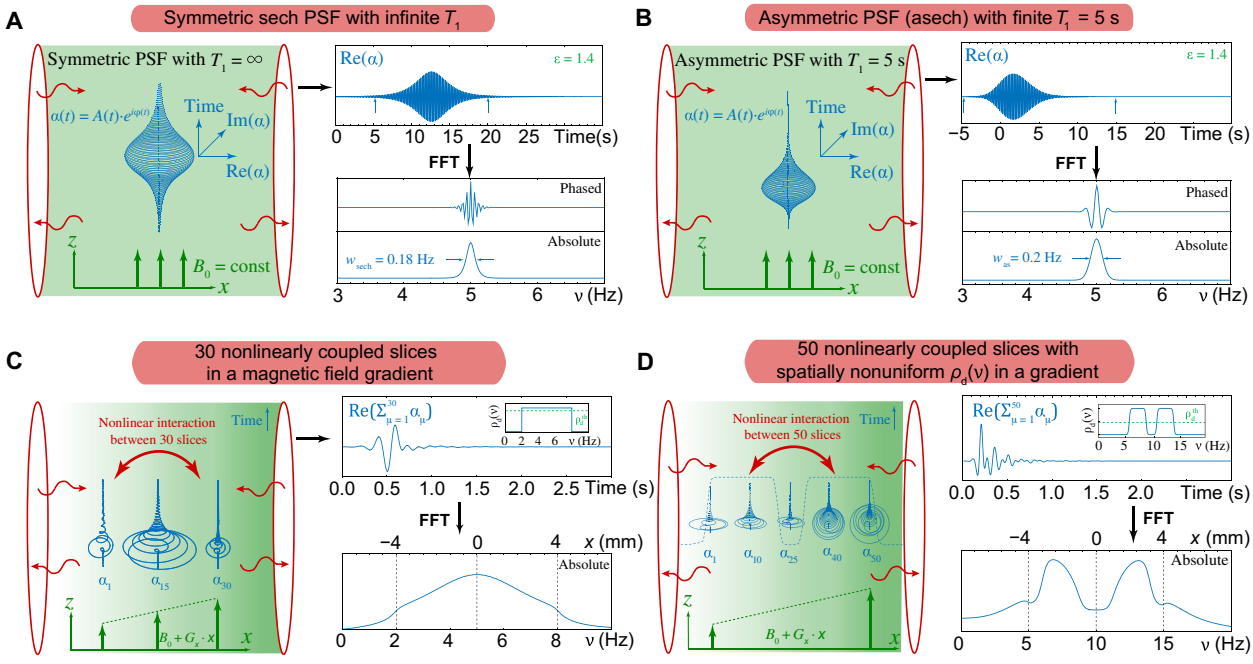

Fig. 1. Simulated RASER signals and the corresponding Fourier-transformed spectra for different numbers of interacting slices. The nonlinear interaction between all slices is mediated by the virtual photons (wavy arrows, wavelength ≫ sample dimension) in the resonator (red) (*51*). After the RASER burst, the Zeeman energy of the spins is fully transferred to the current of the coil (*52*). (**A**) For $N = 1$ and $T_1 = \infty$, the signal $\alpha_1(t) = \alpha(t)$ is plotted in the [*t*, Re(α), Im(α)] space (left). The projection Re(α) for $d_0 = 4.2 \cdot 10^{15}$ and the corresponding Fourier-transformed spectra are shown on the right. (**B**) For $N = 1$, $T_1 = 5$ s and $d_0 = 4.2 \cdot 10^{15}$, the signal burst $\alpha(t)$ is asymmetric with respect to time. (**C**) Sketch of three representative signals α_μ, where $\mu = 1$, 15, and 30 of $N = 30$ interacting slices [$T_1 = 5$ s, $\Delta = 6$ Hz, rectangular profile with $\rho_d(\nu) = 7.5 \cdot 10^{15}$/Hz]. (**D**) Five representative signals α_μ of $N = 50$ coupled slices [$T_1 = 5$ s, $\Delta = 10$ Hz, nonuniform density $\rho_d(\nu)$]. Threshold population density $\rho_d^{th} = d_{th}/w = 6.6 \cdot 10^{15}$/Hz is indicated as dotted line in the insets in (C) and (D). FFT, fast Fourier transform.

RESULTS

RASER MRI explored by numerical simulation

In the simulation in Fig. 1C, a rectangular polarization profile (inset, top right) is assumed to generate a RASER signal in the presence of a field gradient. The time evolution of three of the $N = 30$ slices is depicted on the left. The shape of signal of these slices differs significantly from the uncoupled PSFs in Fig. 1 (A and B). A corresponding one-dimensional (1D) RASER image (projection) is obtained as the Fourier transform from $\mathrm{Sig}(t) = \mathrm{Re}\left(\sum \alpha_\mu\right)$. The amplitude in the center of the RASER image is larger, and decaying side lobes arise outside of the image boundaries at $x = \pm 4$ mm (bottom right). These artifacts are expected from the theory described in Eqs. 1 to 4 and evaluated in detail by numerical simulations in section S4.

In Fig. 1D, we simulate a RASER image using a spin density profile $\rho_d(\nu)$ to match the experimental setup described in Fig. 2 (A and B). This nonuniform spin density profile $\rho_d(\nu)$ entails two equal compartments separated by a gap. The evolution of five representative RASER slices of $N = 50$ coupled slices is shown (Fig. 1D, left). The image after Fourier transformation (bottom right) reflects roughly the shape $\rho_d(\nu)$ except for the deformed amplitudes of the flat tops and the side lobes, which occur outside the imaging boundaries.

Experimental realization of RASER MRI: 1D demonstrations

To experimentally examine the RASER MRI theory, a simple phantom was prepared consisting of a cylindrical sample chamber divided into two measurement chambers by a glass slide (Fig. 2, A and B). The two chambers are individually supplied with *p*-H_2 to generate highly negative polarized proton spins (i.e., $d_0 \gg d_{th}$). The chemical system chosen is pyrazine in a liquid methanol-d_4 solution with a dissolved iridium-based Signal Amplification By Reversible Exchange (SABRE) catalyst for nuclear spin polarization (*18*, *41*). RASER magnetic resonance image were acquired in the presence of weak G_x and G_z magnetic field gradients on the order of a few milligauss per centimeter.

Conventional magnetic resonance images were obtained with a spin echo sequence of 90° followed by a 180° rf pulse (Fig. 2C) as a reference. Before the acquisition of the reference spin echo image (SEI), a crusher field gradient was applied to the hyperpolarized sample, to suppress spontaneous RASER buildup. 1D images were acquired using the G_z gradient to visualize the two chambers separated by the dividing glass slide. 2D images were recorded through stepwise switching of the G_x and G_z gradients to rotate through a circle with constant absolute gradient [$|G| = (G_z^2 + G_x^2)^{1/2}$]. The 2D image was then obtained via projection reconstruction, which is also common in computed tomography.

The RASER images were acquired in a similar way (Fig. 2D), but in contrast to the spin echo sequence, no RF pulses were applied. The signal is acquired in the presence of G_x and G_z field gradients during spontaneous RASER emission, which begins shortly after the crusher field gradient is turned off.

The RASER action can be measured over an indefinite period (Fig. 3A), when *p*-H_2 is continuously bubbled through the solution. However, the bubbling-induced sample motion in the presence of field gradients is a challenge for imaging. The motion collapses the RASER spectrum in each chamber into one average frequency (Fig. 3B). To avoid line collapse induced by sample motion and to

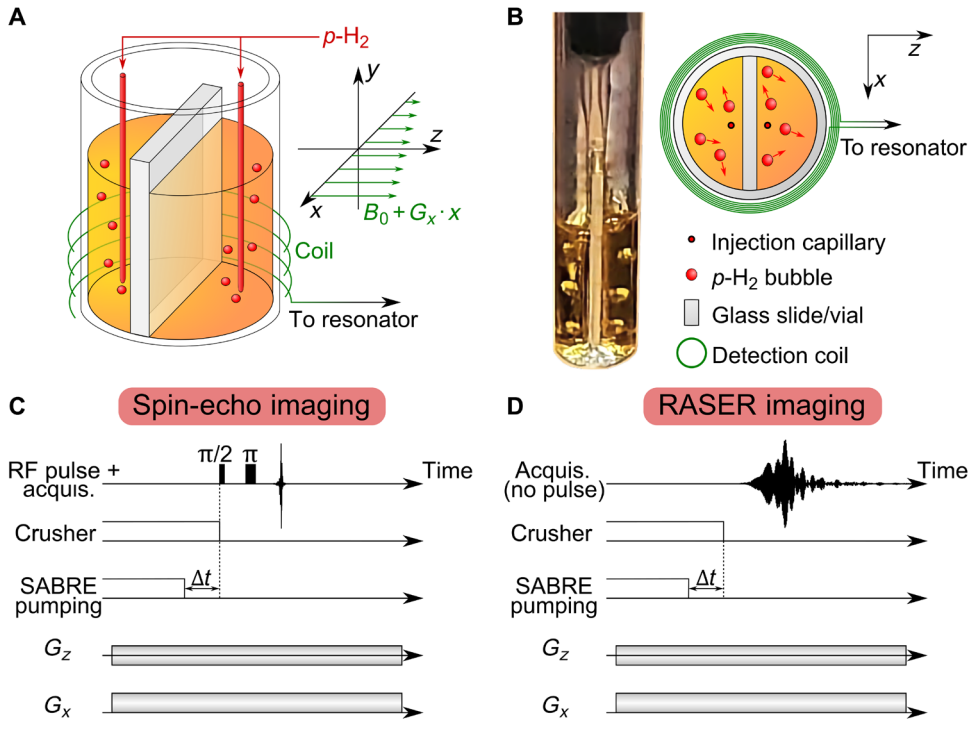

Fig. 2. Experimental setup for MRI of a two-chamber phantom and corresponding pulse sequences for SEI and RASER MRI. (**A**) Schematics of the two imaged chambers and of the gradient directions. (**B**) Photo and top-down schematic of the two chambers (L = 8 mm in diameter and 10 mm in height separated by a 1-mm-thick glass slide) including bubbling of p-H_2 through two capillaries [100 μm in outer diameter (OD) and 30 μm in inner diameter (ID)]. (**C**) Spin echo sequence of 90° followed by a 180° rf pulse for SEI. (**D**) RASER imaging sequence. For both imaging sequences, a crusher gradient is applied to destroy all coherence, while negative proton polarization is built up by SABRE pumping at magnetic fields B_0 of 3.9 and 7.8 mT. p-H_2 bubbling is interrupted to allow the solution to settle for a time Δt. For SEI, the image is encoded in the echo signal. In the case of RASER MRI, the signal builds up spontaneously in the absence of any RF excitation. Frequency encoding is performed in the x and z directions.

enable imaging, the p-H_2 flow had to be stopped and an additional waiting time Δt was introduced, which allows for the solution to settle and the motions to halt. Now, both spin echo and 1D RASER signals could be acquired (Fig. 3, D and G) shortly after the crusher gradient was switched off. The acquired RASER burst in Fig. 3G is significantly longer than the corresponding spin echo in Fig. 3D acquired at the same gradient strength of G_z = 3.84 mG/cm.

The spatial resolution limit is given by $\delta z = w/(\gamma_H \cdot G_z)$ in conventional MRI (*22*). This limit yields δz_{SEI} = 280 μm for the SEI in Fig. 3E, and as a result, the gap and the edges of the sample are not well resolved. However, for RASER 1D projection in Fig. 3H, the slope at the image boundaries at the gap is more than three times steeper. This corresponds to an estimated spatial resolution of $\delta z_{RI} \approx$ 90 μm. However, care has to be taken with this comparison because the contrast mechanism for RASER MRI is based on collective and nonlinear interaction. Spatial resolution might not be a suitable measure for the observed hole in Fig. 3H. Instead, we examine the sensitivity of RASER MRI to local variation in the object $\rho_d(v)$ compared to the sensitivity of conventional MRI to local variations in the object. Simulations support that RASER MRI is more sensitive to small local variations in the imaged object (section S4A and fig. S7).

The measured 1D RASER image in Fig. 3H shows signal lobes outside the boundaries of z = −4 mm, in accordance with the simulation shown in Fig. 1D. These artifacts from 1D RASER MRI are analyzed in section S4B, and a potential correction method is proposed.

Experimental realization of RASER MRI: 2D demonstration and comparison to traditional SEI of hyperpolarized solutions

Both a 2D SEI (Fig. 4A) and a 2D RASER MRI (Fig. 4B) of the same sample are obtained, extending 1D imaging to 2D imaging by reconstructing from 30 angular directions. The field gradient used for the SEI was 3.5 times larger than that for RASER MRI to obtain comparable resolution. Each individual projection in the SEI has a resolution of 50 μm, only about an order of magnitude higher than modern microimaging (*42*–*44*). The two semicircle-shaped halves and the 1-mm gap are visible in Fig. 4 (A and B). These images also display typical projection reconstruction star artifacts outside of the imaging domain. The 2D RASER image in Fig. 4B not only shows sharper features but also exhibits a deformed shape of the sample and its gap, paired with several interfering lines. These lines could be caused by the nonlinear interaction between the slices, analogous to features observed during strong radiation damping at high magnetic field (*45*). An alternative reason could be the residual motion in the liquid after turning off the p-H_2 pumping. These artifacts can be identified in the individual 1D projections, which are used to reconstruct the 2D RASER image (see fig. S11).

RASER MRI dependence on polarization

A stark contrast of RASER MRI to traditional MRI is the dependence of RASER MRI images on the magnitude of the nuclear spin polarization. Figure 5 shows a series of 1D RASER images and SEIs

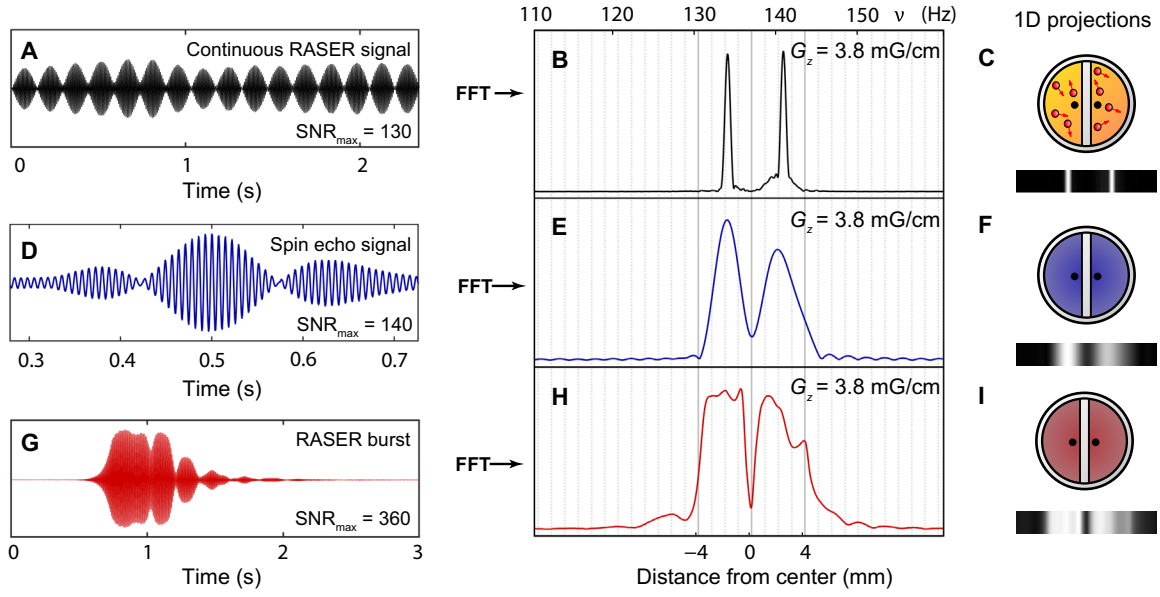

Fig. 3. 1D projections of a continuously pumped proton RASER, a SEI, and a RASER image. (**A**) Continuously SABRE pumped proton RASER signal and corresponding fast Fourier transform spectrum (**B**) in the presence of a gradient G_z. A Hamming window is applied to the signal before fast Fourier transform to suppress sinc wiggles. (**D**) Spin echo acquired with the sequence in Fig. 2C and (**E**) corresponding Fourier-transformed SEI. (**G**) RASER burst acquired with the sequence in Fig. 2D. (**H**) Corresponding RASER 1D projection, which is three times better resolved ($\delta z_{RI} \approx 90$ μm) than the SEI in (E). $B_0 = 7.8$ mT (proton resonance frequency of 333 kHz), and no slice selection is applied. The RASER image (H) has SNR$_{max} = 360$ at $\Delta t = 2$ s, while the SEI in (B) yields SNR$_{max} = 140$ at $\Delta t = 5$ s. All images are phased in the absolute mode and were measured in a single scan. (**C**, **F**, and **I**) Corresponding image phantom and 1D projections.

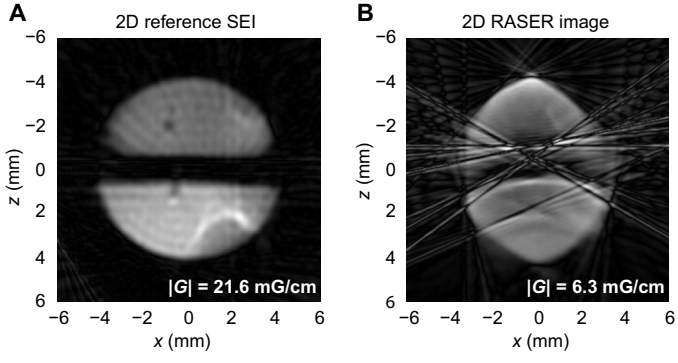

Fig. 4. 2D SEI and 2D RASER image. (**A**) 2D SEI and (**B**) 2D RASER MRI measured at 3.9 mT. The 2D images (A and B) are obtained by projection reconstruction of 30 projections each. These 1D projections are measured with the sequence in Fig. 2 (C and D) from different angles by varying G_x and G_z such that $G_x^2 + G_z^2 =$ constant. In (A), the two capillaries used for p-H_2 supply are visible around $x = -1$ mm, $z = 0.5$ mm and $x = -1.5$ mm, $z = -2$ mm for each chamber. The RASER image (B) is recorded at a 3.5 times smaller gradient than (A), but both spatial resolutions are similar. The RASER image is affected by interference lines. The origin of these artifacts is discussed in the text and in section S5.

of the phantom, acquired with decreasing levels of polarization, i.e., decreasing population inversion d_0. The polarization was adjusted by implementing an increasing waiting time Δt between the polarization step and acquisition.

For SEI, decreasing polarization entails decreasing SNR for each image in Fig. 5A, but the shape of the image in the interval of $2\text{ s} < \Delta t < 20$ s (about a few T_1 relaxation periods) remains invariant. The spatial resolution for the SEI is determined by the slope on the sample boundaries with $\delta z_{SEI} \approx 50$ μm. This observation is in overall good agreement with the theoretical expectation of $\delta z_{SEI} = w/(\gamma_H \cdot G_z) = 55$ μm. Although the initial negative polarization (d_0) changes by more than a factor 10 within the first 20 s, the shape of the SEIs is invariant. This behavior exists because the widths of the underlying PSFs barely deviate from a Lorentzian linewidth and radiation damping effects are insignificant. At longer waiting times ($\Delta t > 20$ s), noise becomes more dominant, and the shape deteriorates as more efficient relaxation at the walls decreases the image amplitude at the boundaries of the sample.

In contrast, the RASER image shape in Fig. 5B strongly depends on polarization. We attribute the differences between the two image halves to disparities in the bubbling rates and phantom shapes (see section S4C). In the case of low polarization ($\Delta t > 15$ s), the maximum amplitude of the right half of the sample is substantially smaller, because the population inversion density $\rho_d(\nu)$ is closer to the RASER threshold density ρ_d^{th}. Because of the collective and nonlinear nature of the contrast mechanism, the slightly larger $\rho_d(\nu)$ of the left half substantially suppresses the amplitude on the right half. This asymmetry in amplitude is much less pronounced if $\rho_d(\nu)$ is further above ρ_d^{th}, for example, at a weaker gradient G_z as in Fig. 3H. Figure 5C shows simulated RASER images for five different initial population inversions d_0 and corresponding profiles $\rho_d(\nu)$ (see fig. S10) to examine the origin of the RASER image distortions. The experiment at $\Delta t = 8$ s matches the simulation with only one peak (width = 0.6 Hz; fig. S9), and for the experiments $\Delta t < 8$ s, the simulation qualitatively reflects the amplitude deformations and side lobes seen in the measured images. The ripples in some images in Fig. 5B cannot be simulated assuming a uniform division of the RASER image into $N = \Delta/\delta\nu$ slices. Motional artifacts and variations

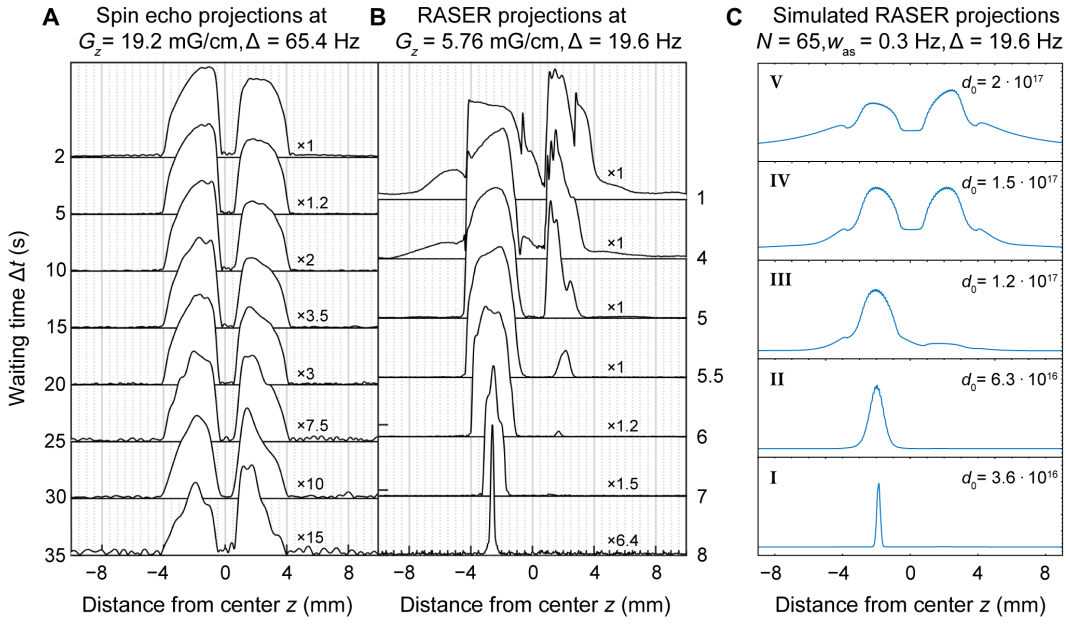

Fig. 5. Projections of measured SEI, RASER MRI at B_0 = 7.8 mT, and simulated RASER MRI at different waiting times Δ*t*. (**A**) The SEI was acquired at G_z = 19.2 mG/cm (δz_{SEI} = 0.055 mm) without slice selection. The shape remains form invariant up until Δ*t* = 20 s. (**B**) The 1D RASER image was acquired at G_z = 5.76 mG/cm. At higher polarizations, i.e., for Δ*t* < 5 s, both sides of the image are governed by strong nonlinear effects. At lower polarization, Δ*t* > 5 s, the amplitude of the right half in the phantom is strongly attenuated. At Δ*t* = 8 s, the RASER image is reduced to one peak of 0.6 Hz width. (**C**) Simulated RASER images, based on Eqs. 1 to 4 and on a profile $\rho_d(v)$ similar to the SEI in (A). These reflect the basic features at different values d_0 (I to V), i.e., side lobes outside of the imaging domain and nonlinear deformations. All spectra are phased in absolute mode and normalized to the maxima of each image.

of T_1, T_2*, and B_1 field over the image domain may be responsible for the observed ripples.

DISCUSSION

The proof-of-principle experiments provided here and the corresponding nascent theoretical framework motivate several new challenges and may provide an opportunity to explore the power of alternative contrast mechanisms provided by RASER MRI. A high sensitivity with respect to local variations in the input profile was found, which is based on collective nonlinear interactions between all regions of the sample. There is negligible background signal from other protons (e.g., water or solvent) in RASER experiments. At low magnetic fields (4 and 8 mT are demonstrated here), the RASER signal is many orders of magnitude larger compared to the signal of the more abundant background protons with low Boltzmann polarization. At higher magnetic fields (1.4 T) in RASER NMR spectroscopy, no proton background signals of water were observed because the RF from the RASER active protons does not excite the chemically shifted water protons (*46*). Further potential advantages are the absence of external RF excitation (*27*) (e.g., caused by the transmission coil), which imply minimal specific absorption rate, avoiding unintended heat deposition. In addition, RASER MRI can produce sufficient contrast with weaker magnetic field gradients, reducing potential concerns over peripheral nerve stimulation (*47*). This is a relevant concern if in vivo translation is possible. Last, the RASER MRI theory is connected to many seemingly disjunct systems in science and technology. The developed system of differential equation (Eqs. 1 to 4) and its solutions for the RASER MRI model are equivalent to the fundamental equations in many other fields with prominent examples in synergetics (*15*) and nonlinear dynamics (*14*, *36*, *48*, *49*). We point the interested reader to section S6, where several of those analogies are detailed.

MATERIALS AND METHODS

Sample preparation and setup

SABRE samples were prepared under Schlenk conditions. The samples contained 5 mM SABRE catalyst precursor [Ir(cyclooctadiene)(1,3-bis(2,4,6-trimethylphenyl)imidazole-2-ylidene)Cl] (*41*), and c_{pyr} = 100 mM pyrazine in methanol-d_4. Pyrazine was chosen because it is associated with a single resonance in the NMR spectrum with $n_{s(pyr)}$ = 4 chemically and magnetically equivalent protons, ideal for RASER and SEI experiments. Three hundred microliters were filled into each chamber, giving a total sample volume V_s = 600 μl. A glass capillary [~100 μm in outer diameter (OD) and 30 μm in inner diameter (ID)] was introduced into each chamber for parallel p-H_2 supply. During polarization buildup, p-H_2 was bubbled through the solution at a flow rate of ~30 sccm and at pressure of 2 bar. p-H_2 was generated using a Bruker p-H_2 generator at 35 K, yielding ~94% enriched p-H_2 gas. The sample is located in a cylindrical glass tube (ID = 8 mm), divided by a glass slide (1 mm in thickness) for two-chamber experiments. The designed phantom is handmade. The 1-mm-thick glass sheet is held in place by chemically resistant glue. The liquid sample inside the two chambers is located in the sensitive volume of a cylindrical NMR detection coil (10 mm in ID and 10 mm in height), which is connected to an external resonator with high quality factor (Q_{ext} = 360 at 166 kHz) for sensitive detection of the NMR or RASER signals (*28*). Typically, a negative pyrazine proton polarization of $P_H \approx -10^{-3}$ to -10^{-2} is achieved in a

magnetic field ranging from 3.9 to 7.8 mT. These chosen magnetic fields are close to the field B_0 = 6.5 mT, where the SABRE ^{1}H polarization for pyridine and similar chemical motives such as pyrazine is maximized (*18*). With respect to RASER MRI, low magnetic fields do offer the additional advantage of lower susceptibility artifacts.

Setup-specific parameters

A SABRE-induced ^{1}H polarization of $P_H = -10^{-3}$ corresponds to a population inversion $d_0 = c_{pyr} \cdot V_s \cdot (-P_H) \cdot n_{s(pyr)}\, N_A = 0.1$ mol/l $\cdot$ 6 $\cdot$ 10^{-4} l $\cdot$ $-(-10^{-3})$ $\cdot$ 4, $6.022 \cdot 10^{23}$/mol = $1.4 \cdot 10^{17}$. The total number of ^{1}H spins in the sample is $N_s = 1.4 \cdot 10^{20}$. Analogous calculations yield the initial conditions for simulations in RASER MRI explored by numerical simulation and RASER MRI dependence on polarization and the Supplementary Materials. For example, in Fig. 5, the initial population inversion is assumed to lie between $d_0 = 3.6 \cdot 10^{16}$ and $2 \cdot 10^{17}$. The ^{1}H NMR parameters of pyrazine were measured to be $T_2^* = 0.7$ s (Lorentzian width $w = 1/(\pi T_2^*) = 0.455$ Hz). T_1 values at different positions were measured using the results of the SEIs versus Δt (see Fig. 5A). We found $T_1 = 5.0$ s in the bulk. The measurement close to the walls varied around $T_1 = 2.5 \pm 0.5$ s. For the simulations, we chose a difference in T_1 between the bulk and the walls of 3 s.

The total quality factor of the combined resonator (external resonator and NMR coil) is $Q = 100$. The B_1 field profile from the NMR detection coil in the center of the sample is calculated to be about 10% lower compared to the field at the edges of the sample. As the RASER active slices interact through the B_1 field of the coil, the coupling now depends on space, which is not accounted for in the parameter β in Eqs. 1 to 3. In summary, the dependence of B_1, T_2^*, and T_1 on the location of the sample is the major sources for RASER imaging artifacts. Correction algorithms for artifacts are state of the art for high-field MRI scanners (*50*) and could mostly be adapted to the artifacts presented here. The magnetic fields of the low-cost MRI system are generated by a set of four handmade shim gradients (G_x, G_y, G_z, and G_{crush}) and an electromagnet producing a constant field in the range of 0.5 mT < B_0 < 20 mT. For our experiments, we chose B_0 = 3.9 and 7.8 mT corresponding to 166.6- and 333.3-kHz ^{1}H resonance frequency, respectively. The reference frequency of the spectrometer is chosen such that the off-resonance frequency ν_0 is between 20 and 150 Hz away from the ^{1}H resonance frequency. The homogeneity of the B_0 field is 1 part per million (ppm)/cm^3. The p-H_2 supply in a low-field electromagnet in conjunction with sensitive external high-quality-factor enhanced (EHQE) detection avoids the necessity of a shuttling system for rapid transport of the sample into a high-field magnet. The G_x and G_z gradients were used to obtain projections from 30 different angles (in 6° steps). All data were acquired in a single scan. SEIs were acquired at an echo time of 1 s. 2D images were obtained after projection reconstruction of the 1D slices using a MATLAB code, written for this project. The spatial resolution is divided into a resolution along a slice in radial and angular direction. The radial resolution is 50 μm for SEI at 21.6 mG/cm, which corresponds to 160 points along the 8-mm sample diameter. The angular resolution with 30 slices spanning 180° is 6°.

There are frequency shifts due to slow magnetic B_0 field drifts in the order of a few ppm per minute. At 333 kHz (7.8 mT), these drifts on a time scale of 10 min were more pronounced compared to 166 kHz (3.9 mT). The reason is thermal instability of the current supply in conjunction with heating of the resistive B_0 field coil. For one 1D RASER image measured at 7.8 mT with a corresponding RASER burst lasting a few seconds, a drift of a ppm per minute means less than 0.1 ppm or 0.03-Hz frequency drift. The image domain Δ is typically chosen between 10 and 100 Hz (corresponding to about 20 to 200 slices for SEI), so the drift for a single 1D RASER image is negligible. For a 2D RASER image with a total measuring time of about 30 min for all 30 1D slices, the central frequency between the individual 1D slices could differ by a few Hz. Thus, each 1D image was shifted to yield the same center frequency for all 1D images before projection reconstruction.

Simulation details

The simulations based on the model Eqs. 1 to 4 were performed using Mathematica 8. The NDSolve[] routine was used for the numerical evaluation of the variables $d_\mu(t)$, $A_\mu(t)$, and $\phi_\mu(t)$. The computation time of the system eqs. S5 to S8 can be quite long depending on the number of modes N. All parameters d_μ, A_μ, and ϕ_μ are coupled in between each other in a nonlinear way by the cos and sin terms on the right sides of eqs. S5 to S7. This is the reason for many nonlinear phenomena, which can arise in this RASER MRI model, ranging from phase locking, collapse phenomena, nonlinear image distortions, and edge effects to multiple-period doubling and chaos. While there are exactly N coupling terms for A_μ and ϕ_μ in eqs. S6 and S7, the number of coupling terms for d_μ in Eq. S5 is $N(N-1)/2$. For larger numbers of slices, $N > 100$, the system of equations becomes elaborate and a large amount of computation is required. The computation time is roughly proportional to N^3, so the system eqs. S5 to S7 is classified as a polynomial problem. A typical numerical evaluation using a personal computer takes about 60 s for $N = 50$ and can be many hours to days for $N > 100$.

For these simulations, initial conditions for $d_\mu(0)$, $A_\mu(0)$, and $\phi_\mu(0)$ are required. The initial conditions for $d_\mu(0)$ at $t = 0$ were calculated for a given profile $\rho_d(v)$ (Eq. 4). For $N_s = 1.4 \cdot 10^{20}$ ^{1}H spins, the average value for the initial spin noise amplitude is $\langle A \rangle \sim (N_s)^{1/2} = 1.18 \cdot 10^{10}$ with a random phase $\phi_\mu(0)$. For the simulations, constant values were assumed for simplicity [i.e., $A_\mu(0) = 10^{12}$ and $\phi_\mu(0) = 0$] because the RASER image is independent from the initial transverse spin components [see invariance principle (III) in Introduction and section S1).

SUPPLEMENTARY MATERIALS

Supplementary material for this article is available at https://science.org/doi/10.1126/sciadv.abp8483

REFERENCES AND NOTES

1. M. G. Richards, B. P. Cowan, M. F. Secca, K. Machin, The ^{3}He nuclear Zeeman maser. *J. Phys. B. At. Mol. Opt.* **21**, 665–681 (1988).
2. T. E. Chupp, R. J. Hoare, R. L. Walsworth, B. Wu, Spin-exchange-pumped ^{3}He and ^{129}Xe Zeeman masers. *Phys. Rev. Lett.* **72**, 2363–2366 (1994).
3. H. Gilles, Y. Monfort, J. Hamel, ^{3}He maser for earth magnetic field measurement. *Rev. Sci. Instrum.* **74**, 4515–4520 (2003).
4. D. J. Marion, G. Huber, P. Berthault, H. Desvaux, Observation of noise-triggered chaotic emissions in an NMR-maser. *Chem Phys. Chem.* **9**, 1395–1401 (2008).
5. P. Bösiger, E. Brun, D. Meier, Solid-state nuclear spin-flip maser pumped by dynamic nuclear polarization. *Phys. Rev. Lett.* **38**, 602–605 (1977).
6. A. G. Zhuravrev, V. L. Berdinskiĭ, A. L. Buchachenko, Generation of high-frequency current by the products of a photochemical reaction. *JETP Lett.* **28**, 140 (1978).
7. H. Y. Chen, Y. Lee, S. Bowen, C. Hilty, Spontaneous emission of NMR signals in hyperpolarized proton spin systems. *J. Magn. Reson.* **208**, 204–209 (2011).
8. E. M. M. Weber, D. Kurzbach, D. Abergel, A DNP-hyperpolarized solid-state water NMR MASER: Observation and qualitative analysis. *Phys. Chem. Chem. Phys.* **21**, 21278–21286 (2019).
9. M. A. Hope, S. Björgvinsdóttir, C. P. Grey, L. Emsley, A magic angle spinning activated ^{17}O DNP raser. *J. Phys. Chem. Lett.* **12**, 345–349 (2021).
10. S. Appelt, G. Wäckerle, M. Mehring, Deviation from Berry's adiabatic geometric phase in a ^{131}Xe nuclear gyroscope. *Phys. Rev. Lett.* **72**, 3921–3924 (1994).

11. T. W. Kornack, R. K. Ghosh, M. V. Romalis, Nuclear spin gyroscope based on an atomic comagnetometer. *Phys. Rev. Lett.* **95**, 230801 (2005).
12. S. Appelt, A. Kentner, S. Lehmkuhl, B. Blümich, From LASER physics to the para-hydrogen pumped RASER. *Prog. Nucl. Magn. Reson. Spectrosc.* **114–115**, 1–32 (2019).
13. V. V. Soshenko, S. V. Bolshedvorskii, O. Rubinas, V. N. Sorokin, A. N. Smolyaninov, V. V. Vorobyov, A. V. Akimov, Nuclear spin gyroscope based on the nitrogen vacancy center in diamond. *Phys. Rev. Lett.* **126**, 197702 (2021).
14. S. H. Strogatz, *Nonlinear Dynamics and Chaos: With Applications to Physics, Biology, Chemistry, and Engineering* (Avalon Publishing, 2014).
15. H. Haken, *Synergertics: An Introduction* (Springer-Verlag, 1983).
16. S. Appelt, S. Lehmkuhl, S. Fleischer, B. Joalland, N. M. Ariyasingha, E. Y. Chekmenev, T. Theis, SABRE and PHIP pumped RASER and the route to chaos. *J. Magn. Reson.* **322**, 106815 (2021).
17. C. R. Bowers, D. P. Weitekamp, Transformation of symmetrization order to nuclear-spin magnetization by chemical reaction and nuclear magnetic resonance. *Phys. Rev. Lett.* **57**, 2645–2648 (1986).
18. R. W. Adams, J. A. Aguilar, K. D. Atkinson, M. J. Cowley, P. I. P. Elliott, S. B. Duckett, G. G. R. Green, I. G. Khazal, J. López-Serrano, D. C. Williamson, Reversible interactions with para-hydrogen enhance NMR sensitivity by polarization transfer. *Science* **323**, 1708–1711 (2009).
19. M. Suefke, S. Lehmkuhl, A. Liebisch, B. Blumich, S. Appelt, Para-hydrogen raser delivers sub-millihertz resolution in nuclear magnetic resonance. *Nat. Phys.* **13**, 568–572 (2017).
20. A. N. Pravdivtsev, F. D. Sönnichsen, J. B. Hövener, Continuous radio amplification by stimulated emission of radiation using parahydrogen induced polarization (PHIP-RASER) at 14 Tesla. *Chem. Phys. Chem.* **21**, 667–672 (2020).
21. B. Joalland, N. M. Ariyasingha, S. Lehmkuhl, T. Theis, S. Appelt, E. Y. Chekmenev, Parahydrogen-induced radio amplification by stimulated emission of radiation. *Angew. Chem. Int. Ed.* **59**, 8654–8660 (2020).
22. P. T. Callaghan, *Principles of Nuclear Magnetic Resonance Microscopy* (Clarendon Press, 1993).
23. P. C. Lauterbur, P. Mansfield, *The Nobel Prize in Physiology or Medicine* (2003); www.nobelprize.org/prizes/medicine/2003/summary/.
24. A. Vlassenbroek, J. Jeener, P. Broekaert, Radiation damping in high resolution liquid NMR: A simulation study. *J. Chem. Phys.* **103**, 5886–5897 (1995).
25. Y. Y. Lin, N. Lisitza, S. Ahn, W. S. Warren, Resurrection of crushed magnetization and chaotic dynamics in solution NMR spectroscopy. *Science* **290**, 118–121 (2000).
26. M. T. Pöschko, V. V. Rodin, J. Schlagnitweit, N. Müller, H. Desvaux, Nonlinear detection of secondary isotopic chemical shifts in NMR through spin noise. *Nat. Commun.* **8**, 13914 (2017).
27. N. Müller, A. Jerschow, Nuclear spin noise imaging. *Proc. Natl. Acad. Sci. U.S.A.* **103**, 6790–6792 (2006).
28. M. Suefke, A. Liebisch, B. Blümich, S. Appelt, External high-quality-factor resonator tunes up nuclear magnetic resonance. *Nat. Phys.* **11**, 767–771 (2015).
29. M. P. Augustine, S. D. Bush, E. L. Hahn, Noise triggering of radiation damping from the inverted state. *Chem. Phys. Lett.* **322**, 111–118 (2000).
30. A. Jurkiewicz, Properties and edition of NMR spontaneous maser emission spectra. *Appl. Magn. Reson.* **50**, 709–724 (2019).
31. X. A. Mao, C. H. Ye, Understanding radiation damping in a simple way. *Concept. Magn. Reson.* **9**, 173–187 (1997).
32. M. P. Augustine, Transient properties of radiation damping. *Prog. Nucl. Magn. Reson. Spectrosc.* **40**, 111–150 (2002).
33. V. V. Krishnan, N. Murali, Radiation damping in modern NMR experiments: Progress and challenges. *Prog. Nucl. Magn. Reson. Spectrosc.* **68**, 41–57 (2013).
34. S. H. Strogatz, From Kuramoto to Crawford: Exploring the onset of synchronization in populations of coupled oscillators. *Physica D* **143**, 1–20 (2000).
35. Y. Kuramoto, D. Battogtokh, Coexistence of coherence and incoherence in nonlocally coupled phase oscillators. *Nonlinear Phenom. Complex Syst.* **5**, 380 (2002).
36. Y. Kuramoto, H. Nakao, On the concept of dynamical reduction: The case of coupled oscillators. *Philos. Trans. Royal Soc. A* **377**, 20190041 (2019).
37. X. A. Mao, C. H. Ye, Line shapes of strongly radiation-damped nuclear magnetic resonance signals. *J. Chem. Phys.* **99**, 7455–7462 (1993).
38. X. A. Mao, J. X. Guo, C. H. Ye, Nuclear-magnetic-resonance line-shape theory in the presence of radiation damping. *Phys. Rev. B* **49**, 15702–15711 (1994).
39. D. J. Y. Marion, P. Berthault, H. Desvaux, Spectral and temporal features of multiple spontaneous NMR-maser emissions. *Eur. Phys. J. D* **51**, 357–367 (2009).
40. V. Henner, H. Desvaux, T. Belozerova, D. J. Y. Marion, P. Kharebov, A. Klots, Collective effects due to dipolar fields as the origin of the extremely random behavior in hyperpolarized NMR maser: A theoretical and numerical study. *J. Chem. Phys.* **139**, 144111 (2013).
41. M. J. Cowley, R. W. Adams, K. D. Atkinson, M. C. R. Cockett, S. B. Duckett, G. G. R. Green, J. A. B. Lohman, R. Kerssebaum, D. Kilgour, R. E. Mewis, Iridium N-heterocyclic carbene complexes as efficient catalysts for magnetization transfer from para-hydrogen. *J. Am. Chem. Soc.* **133**, 6134–6137 (2011).
42. S.-C. Lee, K. Kim, J. Kim, S. Lee, J. H. Yi, S. W. Kim, K.-S. Ha, C. Cheong, One micrometer resolution NMR microscopy. *J. Magn. Reson.* **150**, 207–213 (2001).
43. L. Ciobanu, D. A. Seeber, C. H. Pennington, 3D MR microscopy with resolution 3.7 microm by 3.3 microm by 3.3 microm. *J. Magn. Reson.* **158**, 178–182 (2002).
44. A. J. Ilott, A. Jerschow, Super-resolution surface microscopy of conductors using magnetic resonance. *Sci. Rep.* **7**, 5425 (2017).
45. J. Schlagnitweit, S. W. Morgan, M. Nausner, N. Müller, H. Desvaux, Non-linear signal detection improvement by radiation damping in single-pulse NMR spectra. *Chem. Phys. Chem.* **13**, 482–487 (2012).
46. B. Joalland, T. Theis, S. Appelt, E. Y. Chekmenev, Background-free proton NMR spectroscopy with radiofrequency amplification by stimulated emission radiation. *Angew. Chem. Int. Ed.* **60**, 26298–26302 (2021).
47. J. De Wilde, D. Grainger, D. Price, C. Renaud, Magnetic resonance imaging safety issues including an analysis of recorded incidents within the UK. *Prog. Nucl. Magn. Reson. Spectrosc.* **51**, 37–48 (2007).
48. S. Kaka, M. R. Pufall, W. H. Rippard, T. J. Silva, S. E. Russek, J. A. Katine, Mutual phase-locking of microwave spin torque nano-oscillators. *Nature* **437**, 389–392 (2005).
49. C. Bick, M. Goodfellow, C. R. Laing, E. A. Martens, Understanding the dynamics of biological and neural oscillator networks through exact mean-field reductions: A review. *J. Math. Neurosci.* **10**, 9 (2020).
50. J. T. Vaughan, M. Garwood, C. M. Collins, W. Liu, L. D. Barre, G. Adriany, P. Andersen, H. Merkle, R. Goebel, M. B. Smith, K. Ugurbil, 7T vs. 4T: RF power, homogeneity, and signal-to-noise comparison in head images. *Magn. Reson. Med.* **46**, 24–30 (2001).
51. F. Engelke, Virtual photons in magnetic resonance. *Concepts Magn. Reson. Part A* **36A**, 266–339 (2010).
52. X. A. Mao, Calculation of the energy transferred by radiation damping from nuclear spin system to receiver coil in NMR. *Chem. Phys. Lett.* **756**, 137853 (2020).
53. S. Nadis, All together now. *Nature* **421**, 780–782 (2003).
54. P. Ebrahimzadeh, M. Schiek, P. Jaros, T. Kapitaniak, S. van Waasen, Y. Maistrenko, Minimal chimera states in phase-lag coupled mechanical oscillators. *Eur. Phys. J. Spec. Top.* **229**, 2205–2214 (2020).
55. A. Ruotolo, V. Cros, B. Georges, A. Dussaux, J. Grollier, C. Deranlot, R. Guillemet, K. Bouzehouane, S. Fusil, A. Fert, Phase-locking of magnetic vortices mediated by antivortices. *Nat. Nanotechnol.* **4**, 528–532 (2009).
56. E. N. Lorenz, Deterministic nonperiodic flow. *J. Atmos. Sci.* **20**, 130–141 (1963).

Acknowledgments: S.L. was accepted as a guest scientist in the RWTH Aachen University and acknowledges the university for providing the research environment and equipment to run all experiments of this study at the ITMC (Institute of Technical and Macromolecular Chemistry). S.A. thanks J. Oquendo Mora (S.A.'s wife) for keeping up the moral during difficult situations in the coronavirus disease 2019 pandemic. Excellent cooperative and IT support from S. van Waasen, M. Schiek, and U. Probst from Forschungszentrum Jülich are acknowledged. M. Adams is greatly acknowledged for valuable help in designing the phantom. **Funding:** This work is supported by the Department of Defense CDMRP, W81XWH-20-10576 (to E.Y.C.); National Heart, Lung, and Blood Institute, 1 R21 HL154032-01 (to E.Y.C.); National Science Foundation, CHE-1904780 (to E.Y.C.); National Institute of Biomedical Imaging and Bioengineering, 1R01EB029829 (to E.Y.C. and T.T.); Office of Biological and Environmental Research of the U.S. Department of Energy Atmospheric System Research Program Interagency, agreement grant DE-SC0000001; and National Institute of Health, R21-EB025313 and R01EB029829 (to T.T.). The content is solely the responsibility of the authors and does not necessarily represent the official views of the National Institutes of Health. T.T. acknowledges funding from the Edward Mallinckrodt, Jr. Foundation. SL greatly acknowledges support by the KIT-Publication Fund of the Karlsruhe Institute of Technology.
Author contributions: Conceptualization: S.L. and S.A. Methodology: S.L. and S.A. Software: S.L., L.L., S.F., and S.A. Resources: A.A., T.T., and S.A. Formal analysis: S.L., S.F., L.L., and S.A. Investigation: S.L., S.F., L.L., and S.A. Visualization: S.L., S.F., L.L., T.T., and S.A. Funding acquisition: A.A. and T.T. Project administration: S.A. Writing—original draft: S.L., T.T., and S.A. Writing—review and editing: S.F., L.L., M.S.R., E.Y.C., and A.A. **Competing interests:** T.T. is a founder, equity holder, and president of Vizma Life Sciences LLC (VLS). VLS is developing products related to the research being reported. The terms of this arrangement have been reviewed and approved by NC State University in accordance with its policy on objectivity in research. M.S.R. is a founder and equity holder of VLS. E.Y.C. declares a stake of ownership in XeUS Technologies Ltd. All other authors declare that they have no competing interest.
Data and materials availability: All data needed to evaluate the conclusions in the paper are present in the paper and/or the Supplementary Materials. The raw data are available at https://zenodo.org/record/6606108#.YrtlMS1h2Rs.

Submitted 1 March 2022
Accepted 27 May 2022
Published 13 July 2022
10.1126/sciadv.abp8483

ScienceAdvances

RASER MRI: Magnetic resonance images formed spontaneously exploiting cooperative nonlinear interaction

Sören LehmkuhlSimon FleischerLars LohmannMatthew S. RosenEduard Y. ChekmenevAlina AdamsThomas TheisStephan Appelt

Sci. Adv., 8 (28), eabp8483. • DOI: 10.1126/sciadv.abp8483

Science Advances (ISSN) is published by the American Association for the Advancement of Science. 1200 New York Avenue NW, Washington, DC 20005. The title *Science Advances* is a registered trademark of AAAS.